Snowball Earth Initiation and the Thermodynamics of Sea Ice

Johannes Hörner[1,2] , Aiko Voigt[1] , and Christoph Braun[2]

[1]Department of Meteorology and Geophysics, University of Vienna, Wien, Austria, [2]Institute of Meteorology and Climate Research-Department Troposphere Research, Karlsruhe Institute of Technology (KIT), Karlsruhe, Germany

Abstract Snowball Earth is a hypothesized state in the deep past of Earth in which the ocean was completely or nearly completely covered by sea ice, resulting from a runaway ice-albedo feedback. Here, we address how the treatment of sea-ice thermodynamics affects the initiation of a Snowball Earth in the global climate model ICON-A run in an idealized slab-ocean aquaplanet setup. Specifically, we study the impact of vertical resolution and brine pockets of ice by comparing the 3-layer Winton and a 0-layer Semtner scheme, and we investigate the impact of limiting ice thickness to 5 m. The internal heat storage of ice is increased by higher vertical resolution and brine pockets, which weakens surface melting and increases global albedo by allowing snow and ice to persist longer into the summer season. The internal heat storage weakens the melt-ratchet effect, as is confirmed with offline simulations with the two ice schemes. The result is a substantially easier Snowball Earth initiation and an increase in the critical CO_2 for Snowball initiation by 50%. Limiting ice thickness impedes Snowball initiation as the removal of excess ice leads to an artificial heat source. Yet, the impact is minor and critical CO_2 is decreased by 5% only. The results show that while the sea-ice thickness limit plays only a minor role, the internal heat storage of ice represents an important factor for Snowball initiation and needs to be taken into account when modeling Snowball Earth initiation.

Plain Language Summary Between 500 and 1000 million years ago, there were probably multiple occasions when the oceans of Earth were completely covered by ice. These "Snowball Earth" events are initiated by a growing area of sea ice, which reflects more of the incoming sunlight and thus cools the Earth, up to a point where climate becomes unstable and ice cover becomes global. In this work, we use a global climate model and investigate how the treatment of sea ice in a climate model influences the formation of a Snowball Earth. We find that representing the ice internal heat storage with higher vertical resolution and brine pockets makes it easier to reach a Snowball Earth, because it weakens melting of snow and ice, which brightens the surface and leads to more sunlight being reflected. Additionally, if sea ice is not allowed to grow thicker than 5 m, reaching a Snowball Earth is more difficult because the thin ice results in an artificial heat source that warms the atmosphere. Yet, the impact is small. Taken together, our results show that a high vertical resolution of sea ice is important for realistic investigations of the initiation of Snowball Earth.

1. Introduction

During the Neoproterozoic era from 1000 Ma to 541 Ma ago, Earth was subject to multiple global or nearly global glaciations that are referred to as Snowball Earth (Hoffman et al., 2017; Pierrehumbert et al., 2011). The Snowball Earth pan-glaciations differ from more recent glaciations in Earth history in that ice cover was not limited to mid-latitudes but reached global or near-global levels (Hoffman et al., 1998). Snowball Earth events rank among the most extreme climate states ever experienced by Earth and challenge the survival of early multi-cellular life in the ocean (Runnegar, 2000). They are also relevant for extrasolar planets and their potential habit-ability (Yang et al., 2020). This makes understanding Snowball Earth an important topic for the climate of Earth and other planets, with links to the question of how climate might influence the evolution of life.

The basic mechanism to initiate a Snowball Earth is the well-understood positive ice-albedo feedback: a surface covered by ice is brighter than an ice-free surface and reflects a larger fraction of the incoming solar radiation, because of which an increase in ice cover cools the global climate and leads to further ice growth (Kirschvink, 1992). When ice cover advances toward the equator, the ice-albedo feedback becomes stronger as local insolation at the ice margin increases due to the curvature of Earth. At a certain magnitude of ice cover, the ice-albedo feedback becomes stronger than the stabilizing negative climate feedbacks, and ice growth and fall-ing temperatures enhance each other until global glaciation is achieved. This critical ice latitude and the radiative

forcing at which it occurs mark the location of the bifurcation for Snowball Earth initiation. The critical radiative forcing is often expressed in terms of atmospheric carbon dioxide or the level of insolation.

The location of the bifurcation defines the sensitivity of climate to enter a Snowball state and can be quantified with the help of global climate models. Previous studies reported a wide range of model-based estimates of the Snowball bifurcation. Depending on the model and boundary conditions, these studies reported that Snowball initiation was relatively easy or rather difficult (e.g., Pierrehumbert et al., 2011; Poulsen & Jacob, 2004; Voigt et al., 2011; Voigt & Abbot, 2012; Yang et al., 2012a, 2012b; Y. Liu et al., 2013). Although model studies in isolation are insufficient to "prove" or "falsify" the Snowball Earth hypothesis, they provide a tool to study the climate dynamics of Snowball Earth. They also provide perspectives on factors that govern the initiation of a Snowball Earth, such as continental configuration (Voigt et al., 2011; Y. Liu et al., 2013) and topography (Walsh et al., 2019; Y. Liu et al., 2018), dust (P. Liu et al., 2020), cloud-radiative effects (Voigt & Marotzke, 2010), and the dynamics of the atmosphere and ocean (Poulsen & Jacob, 2004; Rose, 2015; Voigt & Abbot, 2012). Sea-ice dynamics (Lewis et al., 2007; Voigt & Abbot, 2012) and the albedo of sea ice and snow (Abbot et al., 2011; Pierrehumbert et al., 2011; Voigt & Abbot, 2012; Yang et al., 2012b) have been found to be strong controls on the magnitude of the ice-albedo feedback and Snowball Earth initiation.

A factor that has received little attention is the thermodynamics of sea ice. This is surprising because ice thermodynamics should modulate the ice-albedo feedback in a fundamental manner by setting the growth and melt of ice and snow, which affects surface albedo. Yang et al. (2012b) reported that increasing the number of ice layers enhances the ice-albedo feedback, but did not study the reasons for this and did not quantify the impact on the Snowball bifurcation. Abbot et al. (2010) showed, in the context of Snowball termination, that the diurnal cycle and ice surface melting is overestimated when the vertical structure of ice is not properly resolved, that is, when too few ice layers are used. In combination with the neglect of surface melt water, this results in a "melt-ratchet effect": During summer or daytime, melting takes place at the upper ice surface. If ice models remove molten surface water, no refreezing can occur during winter or nighttime. The consequence is a stepwise reduction in ice thickness on a daily and a seasonal scale that is stronger for a stronger diurnal or seasonal cycle.

A further motivation of our work is that previous modeling studies of Snowball initiation often used simplified representations of ice thermodynamics. This includes in particular the work of one of us with the coupled ECHAM5/MPI-OM model that used a 0-layer Semtner scheme for which ice thickness needed to be limited to about 8 m to avoid ocean layers being completely filled with ice, which otherwise would have caused problems in the ocean model (Voigt & Abbot, 2012; Voigt et al., 2011; Voigt & Marotzke, 2010). The studies of Romanova et al. (2006) and Lewis et al. (2007) applied a 0-layer sea-ice scheme without a thickness limit, whereas others like Poulsen and Jacob (2004) and Yang et al. (2012a); Yang et al. (2012b, 2020) applied sea-ice schemes with three or more layers. In other studies that model Snowball Earth climate, the representation of ice thermodynamics is not clear. In investigations of present and future climate, 0-layer sea-ice schemes are used as well, for example, in the CMIP6 model MPI-ESM (Mauritsen et al., 2019) and the ICON-ESM model based on it (Jungclaus et al., 2021). Other CMIP6 models like the IPSL-CM6A-LR model use a 3-layer sea-ice scheme (Boucher et al., 2020).

Both the thickness limitation and a 0-layer scheme might be acceptable for simulations of present-day climate in which ice is restricted to polar latitudes, the diurnal cycle is weak and ice does not grow beyond a couple of meters. However, these assumptions are violated in Snowball simulations. In these, the ice edge enters middle and low latitudes and ice growth to thicker values so that limiting ice thickness might act as an artificial heat source that can impact the bifurcation.

Ice thermodynamics can be expected to shape the bifurcation of Snowball initiation and model estimates thereof, yet no study so far has addressed this impact in a dedicated manner. To clarify the impact of ice thermodynamics on Snowball initiation we compare simulations with two different ice schemes that differ in their vertical resolution, and we conduct simulations in which ice thickness is artificially limited to 5 m. With these simulations we seek to answer two questions:

1. How does the thermodynamical representation of ice, in particular internal heat storage, impact the bifurcation point of Snowball Earth initiation?
2. How does an ice thickness limitation impact the bifurcation point of Snowball Earth initiation?
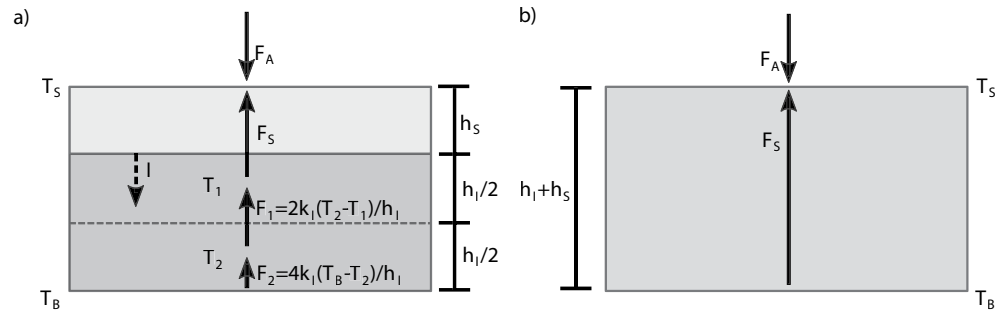
Figure 1. Structure of the 3L-Winton (a) and 0L-Semtner scheme (b).

The paper is organized as follows. Section 2 describes the model setup and simulation strategy and summarizes basic features of the applied ice schemes. Section 3 discusses the impact of internal heat storage, while Section 4 analyses the impact of the thickness limitation. The paper closes with a discussion and conclusion in Section 5.

2. Model Setup

We employ the atmospheric component of the global climate model ICON with the atmospheric physics package developed for climate simulations (ICON-A, version 1.3.00 Giorgetta et al., 2018). To simulate the initiation of a Snowball Earth, we modify ICON-A to run in the idealized aquaplanet configuration (no continents) proposed by Pierrehumbert et al. (2011). The solar constant is set to 1285 W m^{-2} to mimic the weaker Neoproterozoic sun. A circular orbit with an obliquity of 23.5° and a 360-day calendar is applied. The atmosphere is coupled to a mixed-layer ocean with a depth of 50 m without any dynamics or lateral heat fluxes (zero q-flux). All greenhouse gases in the atmosphere are removed except CO_2 and water vapor. Bare and snow-covered ice have an albedo of 0.45 and 0.79, respectively, for a surface temperature of $T_S \leq -1$°C. For warmer temperatures, the albedo values decrease linearly to 0.38 and 0.66 at $T_S = 0$°C, respectively. The albedo values are taken from Abbot et al. (2011). In contrast to Abbot et al. (2011), we do not find waterbelt states with a stable subtropical ice edge for reasons related to clouds (Braun et al., 2022).

The atmospheric model ICON-A is run with a nominal horizontal resolution of 160 km (R2B4). To increase the numerical stability of the model we removed the two topmost model levels so that different from the standard model we apply 45 instead of 47 full levels that extend to a height of 70 instead of 80 km. This does not eliminate all model crashes, especially in extremely cold climates, because of which we further decrease the time step from initially 600–480 s and 360 s when the simulations reach colder climates.

We investigate the location of the Snowball Earth bifurcation by running simulations for different levels of atmospheric CO_2. Most simulations are started from a warm ice-free state that is derived from the AMIP simulations of Giorgetta et al. (2018) and modified for the aquaplanet setup by setting ice cover to zero and making sea surface temperatures zonally symmetric. A few simulations are restarted from other simulations with changed CO_2 (see Figures 2, 3 and 9). We compare the simulations mainly in terms of the latitude of the ice edge and its development over time, based on which we estimate the location of the bifurcation.

We focus on the thermodynamics of sea ice and omit sea-ice dynamics. To this end we compare simulations with the 3-layer scheme of Winton (2000) (3L-Winton in the following) and the 0-layer scheme of Semtner (1976) (0L-Semtner). The 3L-Winton scheme is a reformulated version of the original 3-layer scheme of Semtner (1976) with an energy conserving treatment of brine pockets following Bitz and Lipscomb (1999). The 0L-Semtner scheme is a zero-layer approximation of the original 3-layer scheme. For the 0L-Semtner scheme we also run simulations in which ice thickness is limited to 5 m.

Figure 1 illustrates the 3L-Winton and 0L-Semtner schemes. We first describe the basics of the 3L-Winton scheme and then describe the approximations used in the 0L-Semtner scheme. For a complete documentation of the schemes, the reader is referred to Winton (2000) and Semtner (1976). In this study, we define all heat fluxes as positive toward the interface between the atmosphere and the ice or snow. All atmospheric fluxes are thus positive downward and all internal ice fluxes are positive upward.
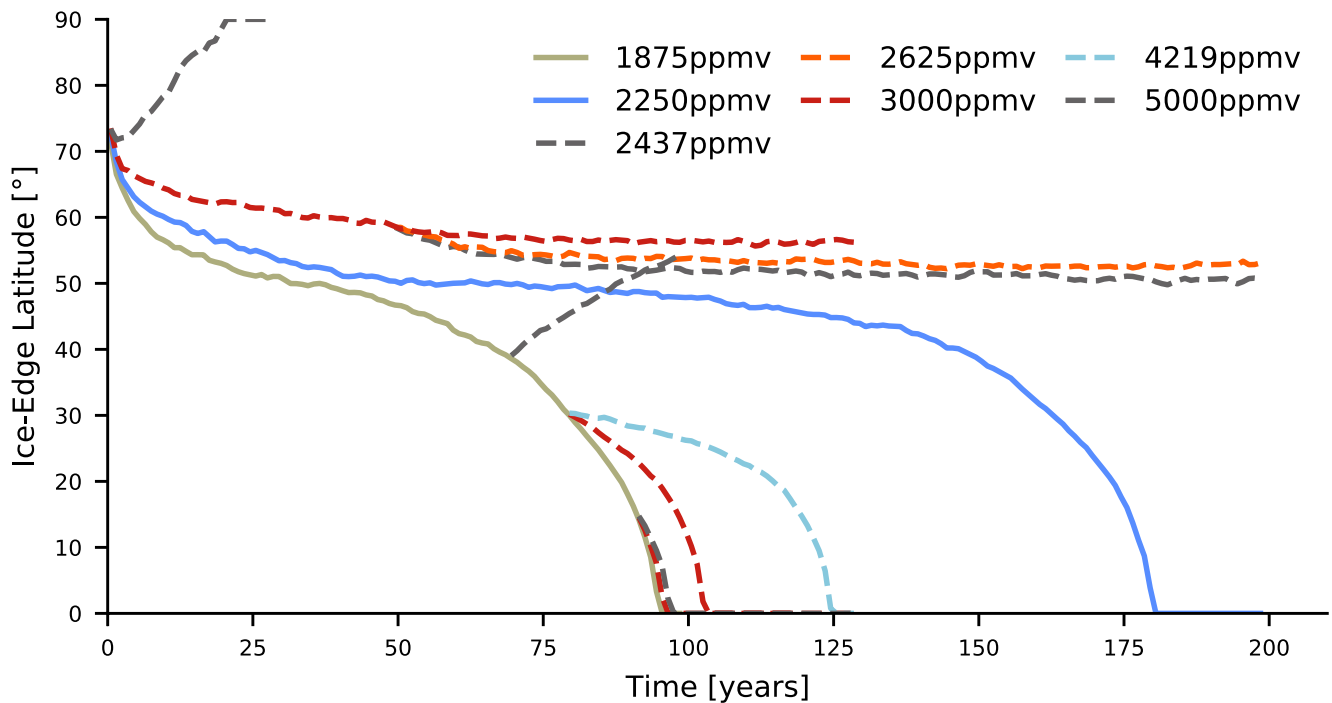
Figure 2. Evolution of the annual-mean ice edge for simulations using the 3L-Winton scheme. Simulations with a higher CO_2 content are plotted with dashed lines to reduce the number of colors.

The 3L-Winton scheme comprises a snow layer with thickness h_S and two ice layers with equal thickness $h_I/2$. The change in surface temperature ΔT_S between two model time steps is obtained from balancing the energy fluxes between the atmosphere and surface on the one hand, F_A, and the conductive heat flux through ice and snow on the other hand, F_S. The longwave radiative flux emitted by the surface is linearized around the surface temperature T_S of the previous time step. F_A is given by
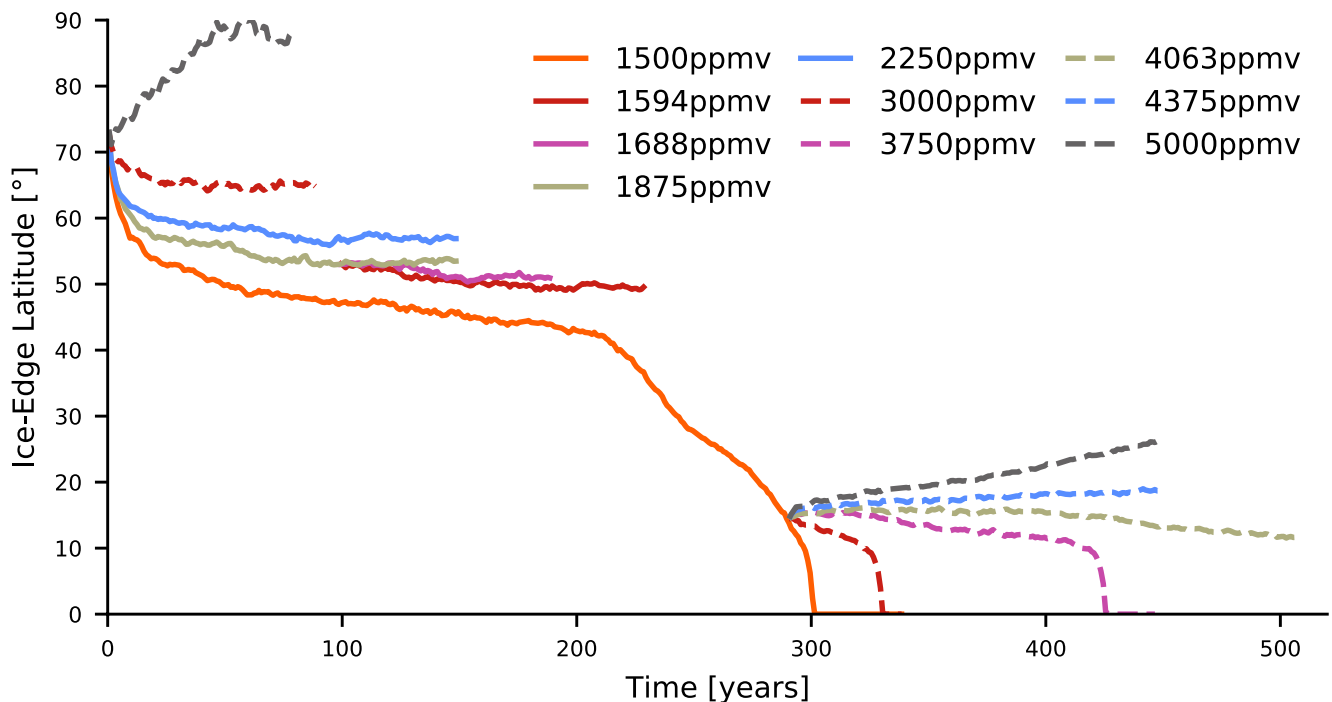

Figure 3. Evolution of the annual-mean ice edge for simulations using the 0L-Semtner scheme. Simulations with a higher CO_2 content are plotted with dashed lines to reduce the number of colors.

$$F_A = F_{lat} + F_{sen} + (1 - I)(1 - \alpha)F_{sw} + \epsilon F_{lw} - \epsilon\sigma T_S^4 - \epsilon 4\sigma T_S^3 \Delta T_S, \tag{1}$$

where all fluxes are defined as positive downward. F_{lat} and F_{sen} denote the latent and sensible heat fluxes; F_{sw} and F_{lw} denote the downward fluxes of shortwave and longwave radiation. α, ϵ and σ are the surface albedo, longwave surface emissivity and the Stefan–Boltzmann constant. If ice is bare, a fraction $I = 0.17$ of the absorbed shortwave radiation penetrates into the ice and heats the upper ice layer instead of increasing the surface temperature. There is no penetrating radiation if ice is snow-covered ($I = 0$).

F_S depends on the temperature T_1 at the midpoint of the upper ice layer,

$$F_S = \frac{T_1 - (T_S + \Delta T_S)}{\frac{h_S}{k_S} + \frac{h_I}{4k_I}}, \tag{2}$$

where $k_{I/S}$ and $h_{I/S}$ are the heat conductivity and thickness of ice and snow, respectively. T_1 is predicted from the difference between F_S and the conductive heat flux through the upper and lower ice layers, F_1, and heating from penetrating solar radiation I,

$$\frac{\rho_I h_I}{2} C \frac{dT_1}{dt} = -F_S + F_1 + I(1 - \alpha)F_{sw}. \tag{3}$$

F_1 involves the temperature of the lower ice layer, T_2, which is predicted from a similar equation. An important feature of the 3L-Winton scheme is that it includes the ability of ice to store heat both via temperature changes and melting and freezing of brine pockets (Untersteiner, 1961). For the upper layer, this is represented by a temperature dependent heat capacity (Appendix A1). For the lower layer, the latent heat storage of brine pockets is neglected and the heat capacity is constant. This is different in the 0L-Semtner scheme for which ice has no heat capacity and no brine pockets.

If the new surface temperature $T_S + \Delta T_S$ is larger than the melting temperature, F_A and F_S are recalculated with the surface temperature set to the melting temperature. The remaining heat flux imbalance is applied as top melting of either ice or snow. The enthalpy of sea ice depends nonlinearly on ice temperature, $E_1(T_1)$, due to the temperature-dependent heat capacity. If no snow is present, the melting of ice is calculated as

$$\frac{dh_I}{dt} = \frac{F_A + F_S}{\rho_I E_1(T_1)}. \tag{4}$$

Otherwise, a constant heat of melting is applied for snow

$$\frac{dh_S}{dt} = \frac{F_A + F_S}{-\rho_S L}. \tag{5}$$

Bottom melting or freezing is calculated from the flux imbalance at the ice-ocean interface. Because lateral ocean heat transport is zero in our study, melting is calculated as

$$\frac{dh_I}{dt} = \frac{-F_2}{\rho_I E_2(T_2)}. \tag{6}$$

The enthalpy of lower-layer sea ice depends linearly on ice temperature, $E_2(T_2)$, as brine pockets are neglected. If one layer is removed completely during one time step, the excess energy is applied toward melting of the second layer. For freezing, the enthalphy of newly formed ice at freezing temperature $E_2(T_f)$ is used. Finally, snow below the waterline is converted to ice and the ice layers are equalized to a thickness of $\frac{h_I}{2}$ each in an enthalpy-conserving way. For more details about these procedures the reader is referred to Winton (2000).

The 0L-Semtner scheme applies additional idealizations. The main difference is that it uses no internal ice and snow layers, which explains its naming as a "zero-layer" model. Thus, in 0L-Semtner ice and snow have no heat capacity and no internal melting of brine, so their temperatures adjust instantaneously according to the flux balance between F_A and F_S.

The 0L-Semtner scheme is defined as follows. F_A is calculated from Equation 1 but with $I = 0$. F_S is not calculated by Equation 2 but directly from the difference between the temperature of the surface T_S and ocean T_B,

$$F_S = \frac{T_B - (T_S + \Delta T_S)}{\frac{h_S}{k_S} + \frac{h_I}{k_I}}. \tag{7}$$

The scheme does not consider brine pockets, so melting and freezing of ice uses a constant latent heating of fusion, $-L$ instead of E (cf. Equation 6). Ice thickness changes from bottom melting or freezing are given by

$$\frac{dh_I}{dt} = \frac{F_S}{\rho_I L}. \tag{8}$$

In ICON-A, a constant heat capacity corresponding to 10 cm thick ice is added in the calculation of the surface temperature in both schemes. This is done to damp surface temperature fluctuations that could arise from, for example, sudden cloud-induced changes in radiative fluxes and does not change the qualitative behavior of the schemes.

3. Vertical Resolution of Ice

In this section, we investigate the impact of the vertical resolution of ice. For this purpose, we compare simulations with the 3-layer Winton (3L-Winton) and 0-layer Semtner schemes (0L-Semtner). In both schemes, ice thickness is unlimited. Figures 2 and 3 show the evolution of the latitude of the ice edge in the simulations.

3.1. Bifurcation Diagram

Figure 4 shows the latitude of the ice edge at the end of all simulations as a function of CO_2.

Snowball initiation is much easier in the 3L-Winton scheme than the 0L-Semtner scheme. Both schemes simulate an ice-free state for a CO_2 value of 5,000 ppmv, for which the treatment of sea ice of course has no impact. Both schemes allow for ice-free and partially ice-covered states as part of the "warm" present-day branch of the bifurcation diagram as well as states with global ice cover that belong to the "cold" hard Snowball branch. Independent of the ice scheme, the present-day branch extends down to an ice edge of 50° latitude. Yet, the schemes differ in the critical radiative forcing. For 0L-Semtner, CO_2 needs to be decreased below 1594 ppmv to trigger Snowball initiation, but only to below 2,437 ppmv for 3L-Winton. The easier initiation in 3L-Winton also leads to a poleward shift of the unstable branch that separates the attractor basins of the present-day and hard Snowball solutions. This so-called separatrix is estimated from non-equilibrated simulations of Figure 4 that we initialized with ice edges equatorwards and CO_2 values above the Snowball bifurcation.

As shown in Figure 4 the Snowball bifurcation point is located at higher CO_2 values for the 3L-Winton scheme. The critical CO_2 is bracketed by the coldest simulation on the present-day branch and the simulation on the Snowball branch with lower CO_2. If we assume that the critical CO_2 value is roughly located in the middle between these two simulations, we find 1547 ppmv for 0L-Semtner and 2,344 ppmv for 3L-Winton, that is, a difference of around 700 ppmv. In relative terms, the 3L-Winton scheme thus initiates a Snowball Earth at a roughly 50% higher CO_2 value than the 0L-Semtner scheme.

3.2. Global Energy Balance and Surface Albedo

To demonstrate how the change in the bifurcation diagram can be traced back to differences in the vertical resolution of the two ice schemes, we compare two simulations with nearly the same ice edge: a 3L-Winton simulation with 2,437 ppmv CO_2 and an ice edge at 50.5°, and a 0L-Semtner simulation with 1688 ppmv CO_2 and an ice edge latitude at 51.1°.

The global mean energy balance at the top of the atmosphere provides a good starting point for the comparison. Both simulations are in global mean energy balance, yet they differ in their CO_2 value. The higher CO_2 in the 3L-Winton simulation means that outgoing longwave radiation is lower compared to the 0L-Semtner simulation (222.2 vs. 223.3 W m^{-2}). Reflected shortwave radiation must thus be higher (98.3 vs. 97.2 W m^{-2}), which
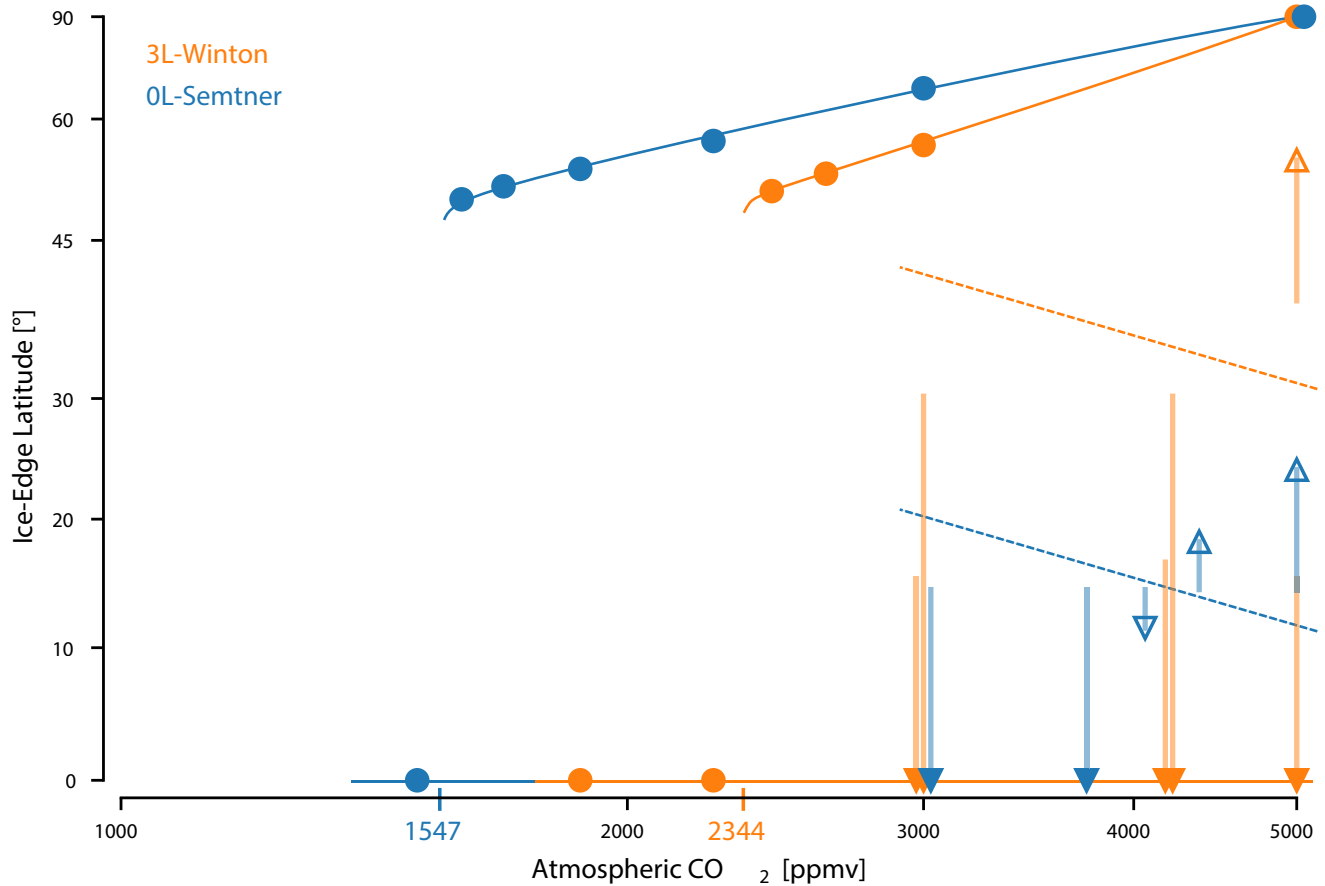
Figure 4. Bifurcation diagram for the 3L-Winton scheme in orange and the 0L-Semtner scheme in blue. Circles indicate the ice edges of equilibrated simulations that were started from a warm climate. Arrows and vertical semi-transparent lines indicate the evolution of the ice latitude from transient simulations, with filled arrows indicating equilibrated states and open arrows indicating non-equilibrated states. The dashes indicate the estimated position of the separatrix. The colored numbers on the x-axis give the estimated critical CO_2 for Snowball initiation. Simulations initiated with the same CO_2 are offset slightly in the horizontal direction for better visibility.

suggests that surface albedo differs between the two simulations. As we will discuss in detail below, the surface albedo difference arise from seasonal ice cover and snow on ice.

Figure 5 shows the zonal mean surface albedo in July for the two simulations. The albedo in the winter hemisphere is very similar since the two simulations exhibit the same ice edge and ice is snow-covered throughout the entire winter hemisphere. In the summer hemisphere, however, the surface albedo in the 0L-Semtner simulation is much lower compared to the 3L-Winton simulation. The difference is strongest in the region of year-round sea ice immediately poleward of 60° latitude but also affects the midlatitude zone of seasonal ice between 40° and 60° latitude. A very similar behavior was found in the 0L-Semtner simulations of a Marinoan Snowball Earth with the coupled model of Voigt and Abbot (2012) (their Figure 6).

The higher surface albedo in 3L-Winton in the summer hemisphere arises from two effects. First, ice tends to be snow-covered and bright in 3L-Winton but bare and hence relatively dark in 0L-Semtner. Second, in the midlatitude region ice exhibits less seasonal variability in 3L-Winton compared to 0L-Semtner, resulting in a larger ice extent during summer but a similar extent during winter.

Figures 6a and 6b illustrates the seasonal reduction of surface albedo due to summer melting. The summer reduction melting is notably smaller in 3L-Winton. 0L-Semtner shows a large area where the surface albedo is decreased, both at latitudes with permanent and seasonal ice cover. The effect of this change in surface albedo can be seen in the outgoing shortwave radiation depicted in Figure 6c. While the radiative difference is small during winter, it starts to increase over the course of the year, first at the ice edge and then reaching its maximum
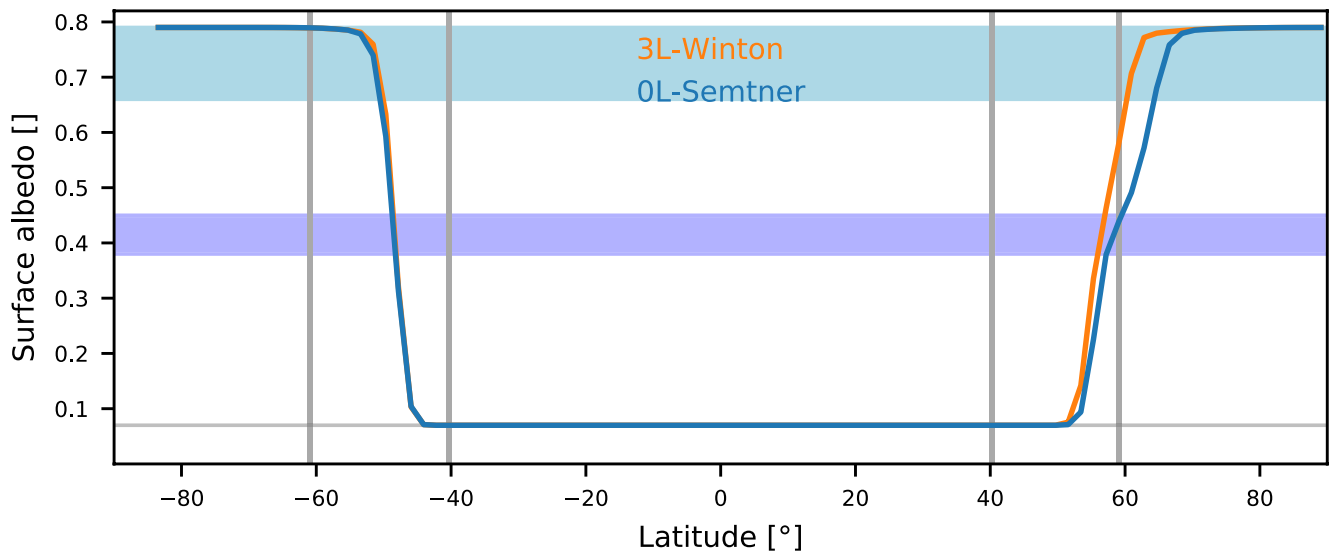
Figure 5. Zonal-mean surface albedo in July averaged over the final 40 years of a 3L-Winton and 0L-Semtner simulation with essentially the same annual-mean ice cover. The 3L-Winton simulation is run with 2,437 ppmv CO_2, the 0L-Semtner simulation with 1688 ppmv. The vertical gray lines illustrate the seasonal cycle of sea ice and separate regions of permanent ice cover, seasonal ice cover and permanent open ocean. The dark and light blue bands indicate the surface albedo range for bare and snow-covered ice.

further poleward during summer. In consequence the 0L-Semtner scheme locally reflects up to 32 $W\,m^{-2}$ less shortwave radiation.

To further assess the impact of surface albedo on the global climate, the annual-mean reflected shortwave radiation is depicted for the two simulations in Figure 7. In clear-sky conditions (no clouds), the differences in the surface albedo are clearly visible and lead to a larger reflection in 3L-Winton. Although clouds dampen the
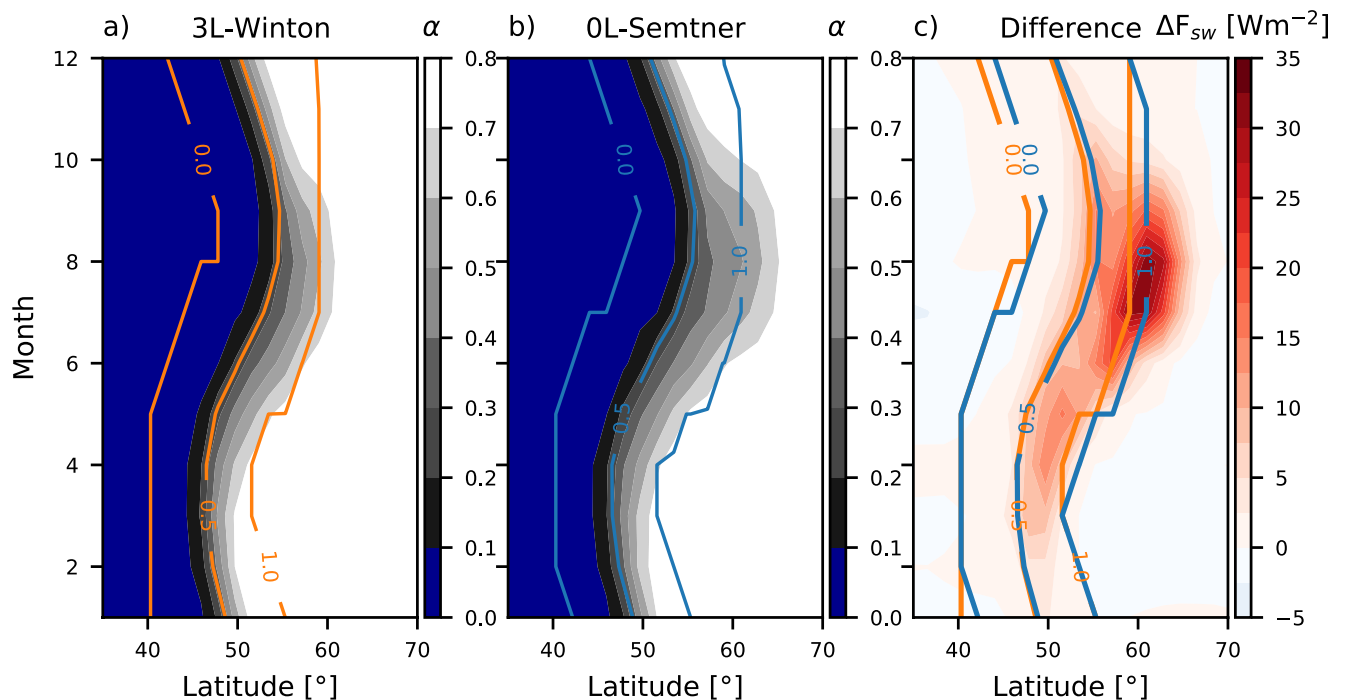

Figure 6. Zonal-mean monthly-mean surface albedo averaged over the final 40 years of the 3L-Winton (a) and 0L-Semtner (b) simulations with the annual-mean ice edge at 51°. (c) Difference in top-of-atmosphere outgoing shortwave all-sky radiation between the two simulations. Contour lines indicate the ice cover.
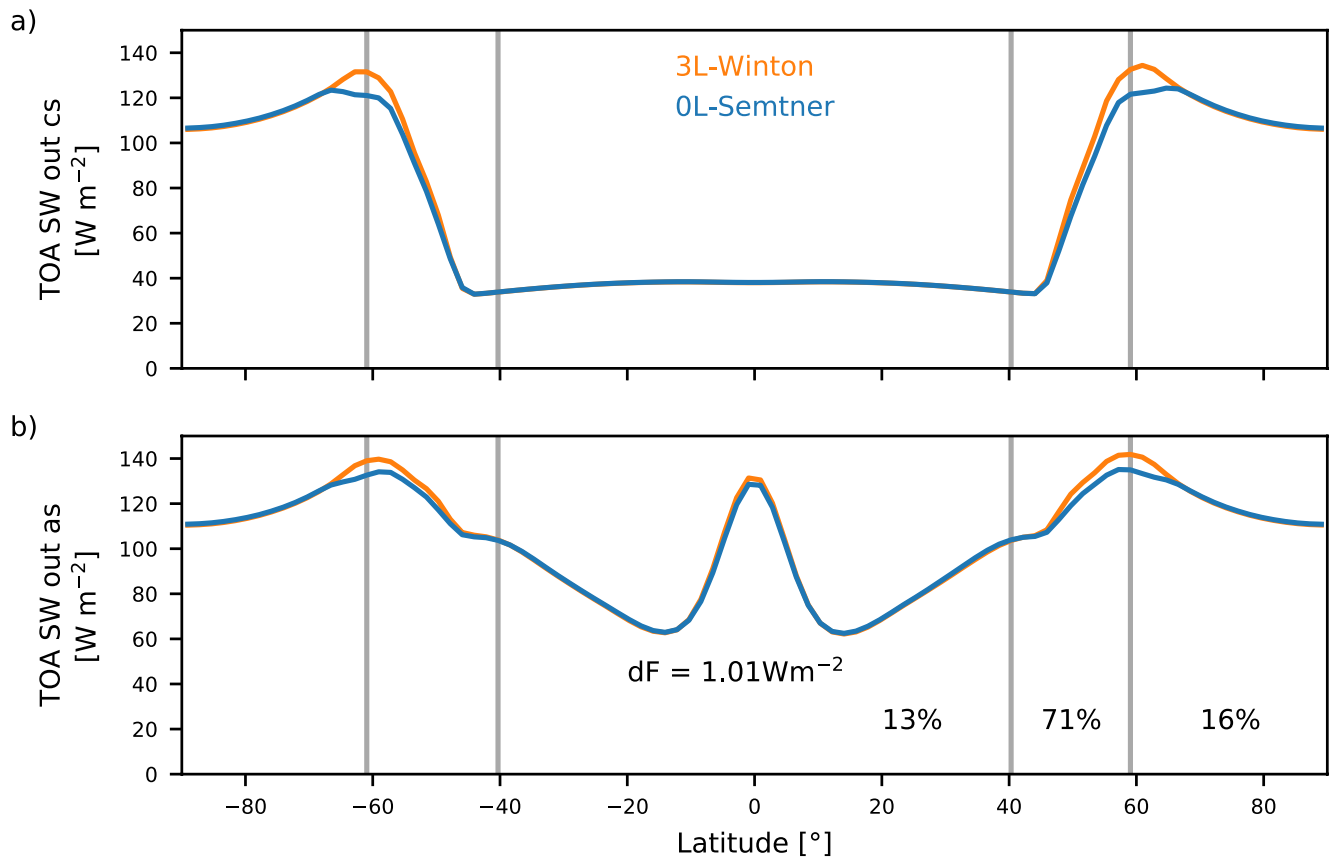
Figure 7. Zonal-mean top-of-atmosphere outgoing shortwave radiation in clear sky (a) and all sky conditions (b) averaged over the final 40 years of simulation for 2,437 ppmv 3L-Winton and 1688 ppmv 0L-Semtner. Vertical gray lines separate permanently ice-covered regions, temporary ice-covered regions and completely ice-free regions. The difference in global shortwave all sky radiation between 3L-Winton and 0L-Semtner is noted in (b), as well as its relative distributed over the three regions.

impact of surface albedo, all-sky reflected shortwave radiation (with clouds) differs between the simulations in the manner expected from the surface albedo difference. In the global annual mean, the 3L-Winton scheme leads to an increase of 1.0 W m^{-2} in reflected shortwave radiation. The majority of this difference ($\approx$70%) stems from the region of seasonal ice cover. This shows the dominant role of differences in seasonal ice melt and snow cover. About 20% stem from permanently ice-covered latitudes, where the presence - or absence - of snow on ice is the responsible factor. The ice free region contributes $\approx$10% due to small difference in tropical clouds that likely arise from the different CO_2 values in the two simulations (Sherwood et al., 2015).

3.3. Offline Simulations With the 3L-Winton and 0L-Semtner Schemes

In this section, we study the physical reasons for the different behavior of ice and snow in the 0L-Semtner and 3L-Winton schemes. We find that the melt-ratchet effect is the dominant reason for the more efficient surface melting of ice and snow, lower surface albedo and hence more difficult Snowball initiation in simulations that use the 0L-Semtner scheme.

To this end, we have re-coded the ice schemes in python, which allows us to run them in offline mode forced with idealized surface fluxes. In the offline mode, the schemes are one-dimensional along the vertical axis. Starting from initial values for ice thickness, snow thickness, surface temperature and—For the 3L-Winton scheme—Internal ice temperatures, the schemes are integrated forward in time and are forced by prescribed idealized energy fluxes at the surface. The time step is set to 600 s. All physical constants are taken from the configuration of the ice schemes as used in ICON-A. The spin-up period is 1 day.
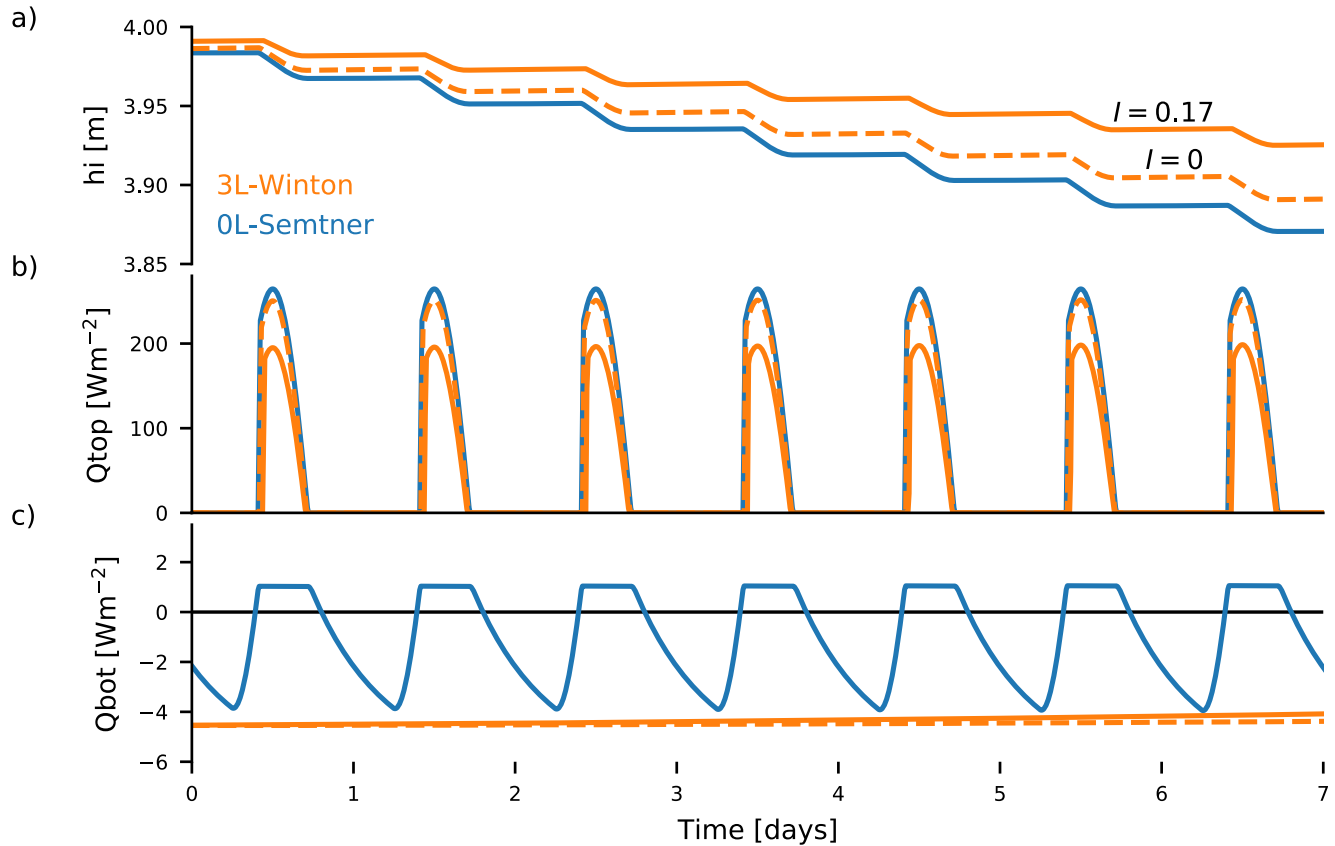
Figure 8. (a) Ice thickness, (b) heat flux for top melting and (c) heat flux for bottom melting in the offline 0L-Semtner and 3L-Winton models. For the 3L-Winton model, dashed lines indicate no penetrating radiation (I = 0) and solid lines a penetrating fraction as used in the ICON-A simulations (I = 0.17). Boundary conditions are identically for both models, consisting of an idealized diurnal cycle of downwelling shortwave radiation and a constant heat flux into the ice surface. A positive heat flux indicates melting and a negative heat flux indicates freezing.

The energy fluxes at the surface are represented by a constant and a sinusoidal term. The constant term $F_{const} = 250\ \mathrm{W\,m^{-2}}$ consists of the incoming longwave radiation, sensible heat, latent heat and the constant part of shortwave radiation. The sinusoidal term $F_{diurnal} = \max\left(600\cos\left(2\pi t\right)\ \mathrm{W\,m^{-2}},\ 0\right)$ represents the diurnal cycle of the shortwave radiation, with t in days. The sum of these fluxes agrees well with the ice surface energy balance observed at the ice border in two simulations with almost identical ice-edge latitudes (3,000 ppmv CO_2 3L-Winton, and 2,250 ppmv CO_2 0L-Semtner). The internal ice temperatures in the 3L-Winton scheme are initialized with $T_1 = -8°C$ and $T_2 = -4°C$. In both schemes, the initial surface temperature is set to $-5°C$ and the initial ice thickness to 4 m. There is no snow on ice.

It should be kept in mind that surface fluxes can change radically in a Snowball Earth simulation. For example, as Earth cools down and transitions into a Snowball Earth the surface fluxes over the sea ice will be negative instead of positive. However, our main concern here is ice near the ice edge that experiences seasonal melting.

The 3L-Winton scheme, as implemented in ICON-A, decreases top melting by a factor of almost two in comparison to the 0L-Semtner scheme. As expected from the large prescribed downward fluxes at the ice surface, both schemes simulate a melting of sea ice (solid lines in Figure 8a). The large positive downward shortwave radiative flux during the day results in a net top heat flux available for melting at the surface (Figure 8b). The 0L-Semtner scheme shows a maximum top heat flux during noon that is 70 $\mathrm{W\,m^{-2}}$ larger than the maximum flux of the 3L-Winton scheme. In the daily average, that is a 50% increase relative to the 3L-Winton scheme (58.2 vs. 37.3 $\mathrm{W\,m^{-2}}$).

Bottom freezing (solid lines in Figure 8c) also differs between the two schemes. In 3L-Winton, bottom freezing decreases over time with rising ice temperatures. In 0L-Semtner, the bottom heat flux oscillates between freezing during night and melting during day, following the diurnal cycle. The daily average in the 0L-Semtner is
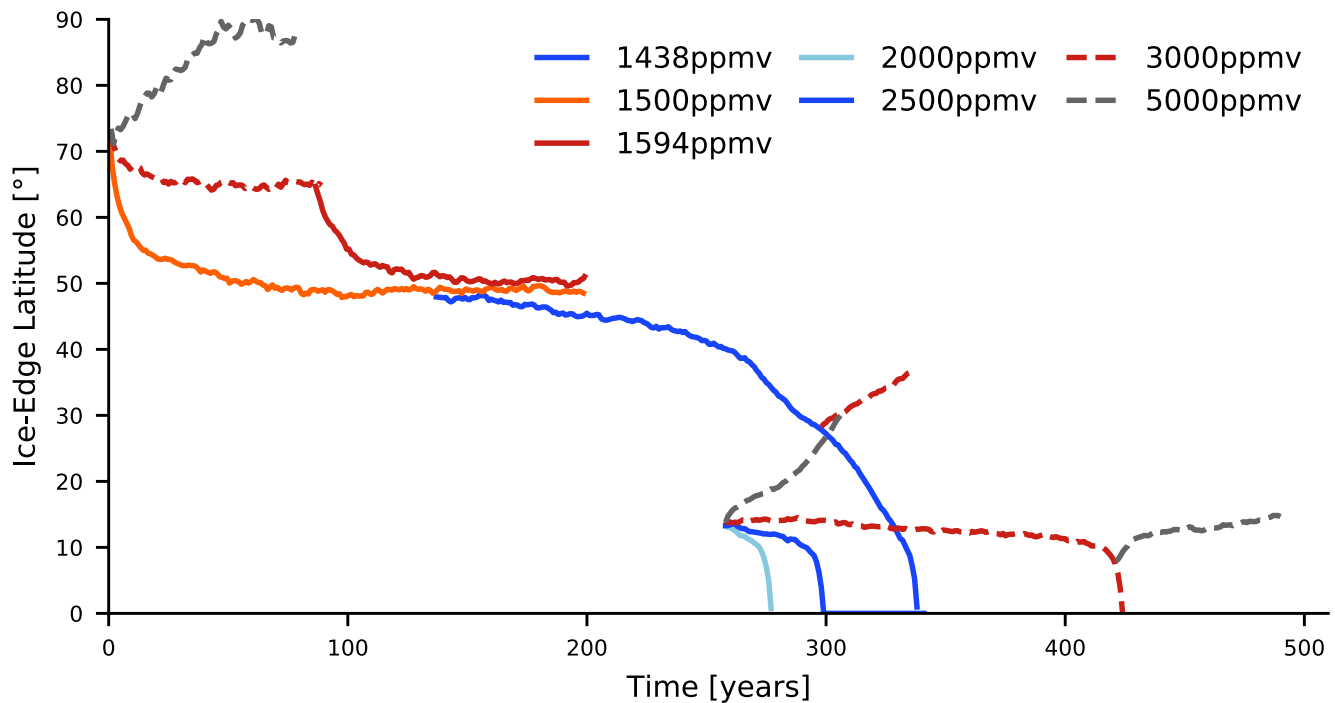
Figure 9. Annual-mean ice edge for simulations using the 0L-Semtner scheme with ice thickness limited to 5 m. Simulations with a higher CO_2 content are plotted with dashed lines to reduce the number of colors.

$-1\,\mathrm{W\,m^{-2}}$ in contrast to $-4\,\mathrm{W\,m^{-2}}$ in the 3L-Winton scheme. The 3L-Winton scheme thus results in larger bottom growth, which adds to the reduced surface melting.

Penetrating shortwave radiation in the 3L-Winton scheme modulates the impact of heat storage, as it diverts a fraction $I = 0.17$ of the energy from the surface toward heating of the upper ice layer if there is no snow on ice. Turning penetrating radiation off ($I = 0$) negates part of the difference in melting, by instantaneously increasing the energy available at the surface (dashed line in Figures 8a and 8b). The energy used for surface melting does not increase the internal heat storage and results in lower ice temperatures. This leads to slightly stronger bottom growth (Figure 8c) and is furthermore expected to cause lower surface melting over long timescales. Ultimately, the ice internal heat storage of the 3L-Winton scheme results in a weaker melt-ratchet effect independently whether penetrating radiation is applied. This confirms the simulation results obtained with ICON-A, where the decreased surface melting is visible both without and with a snow cover (i.e., with and without penetrating radiation, cf. Figure 5).

4. Limiting the Thickness of Sea Ice

In previous studies sea-ice thickness was often limited for technical reasons, for example, to avoid dry levels in the ocean model (see introduction). In this section, we study the impact of such a limit. We compare the 0L-Semtner simulations of Section 3 with unlimited ice thickness to 0L-Semtner simulations in which ice thickness is limited to 5 m. Figure 3 shows the evolution of the latitude of the ice edge for the former set of simulations; Figure 9 shows it for the latter.

4.1. Bifurcation Diagram

We start with the bifurcation diagram shown in Figure 10. For unlimited ice thickness, the figure contains the same 0L-Semtner simulations as Figure 4. The additional 0L-Semtner simulations with limited ice thickness are shown in green.

The impact of limiting ice thickness is small, and in fact much smaller than the impact of increasing vertical resolution. The Snowball bifurcation point is shifted to slightly lower CO_2 when ice thickness is limited. For
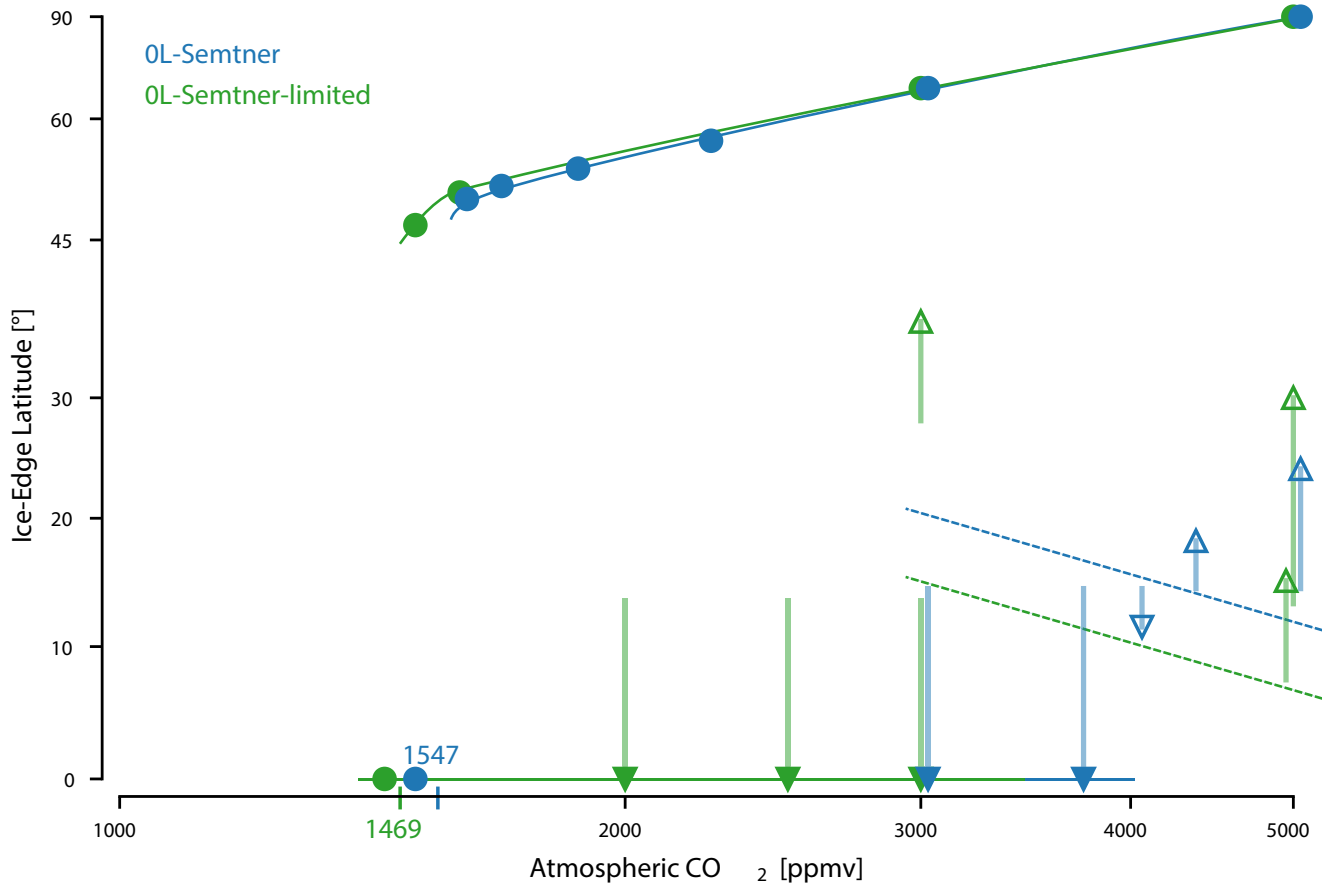
Figure 10. Bifurcation diagram for the 0L-Semtner scheme with unlimited (blue) and limited (green) ice thickness. Circles indicate the ice edges of equilibrated stable states that were started from a warm climate. Arrows and vertical semi-transparent lines indicate the evolution of the ice latitude from transient simulations with different CO_2, with filled arrows indicating equilibrated states and open arrows indicating non-equilibrated states. The dashed indicate the estimated position of the separatrix. The colored numbers on the x-axis give the estimated critical CO_2 for Snowball initiation.

1500 ppmv, a Snowball is initiated for unlimited ice thickness but not for limited ice thickness. For the latter, CO_2 needs to be reduced further to 1438 ppmv. Together with the simulations on the present-day branch with the lowest CO_2, we estimate that the bifurcation point for limited ice thickness is at 1469 ppmv. Limiting ice thickness therefore shifts the bifurcation point to lower CO_2 only by about 80 ppmv, or 5%.

Limiting ice thickness also impacts the evolution of the ice edge. This is shown in Figure 11. At 1500 ppmv CO_2, ice expands in the first 100 years independent of whether its thickness is limited or not. After that point, ice cover in the unlimited simulation continues to expand steadily toward the equator, accelerates after 210 years and reaches a Snowball Earth after 300 years. In contrast, the limited simulation equilibrates with an ice edge near 50° latitude. For 3,000 ppmv CO_2 and an initial ice edge at 14°, the unlimited simulation falls into a Snowball Earth much faster, after 40 years, than the limited simulation, which requires 165 years. For 5,000 ppmv and the same initial subtropical ice edge, ice cover retreats toward the poles in both simulations, but the retreat is much faster when ice thickness is limited.

4.2. Artificial Heat Flux Due to Thickness Limit

The impact of limiting ice thickness arises from an artificial heat flux. At each model time step ice can grow or melt. When ice surpasses the 5 m limit, the excess ice is removed. This corresponds to an artificial heat flux F_r into the ice that is related to the amount of ice $h_{i,r}$ melted due to the thickness limit in accordance to Equation 8 by

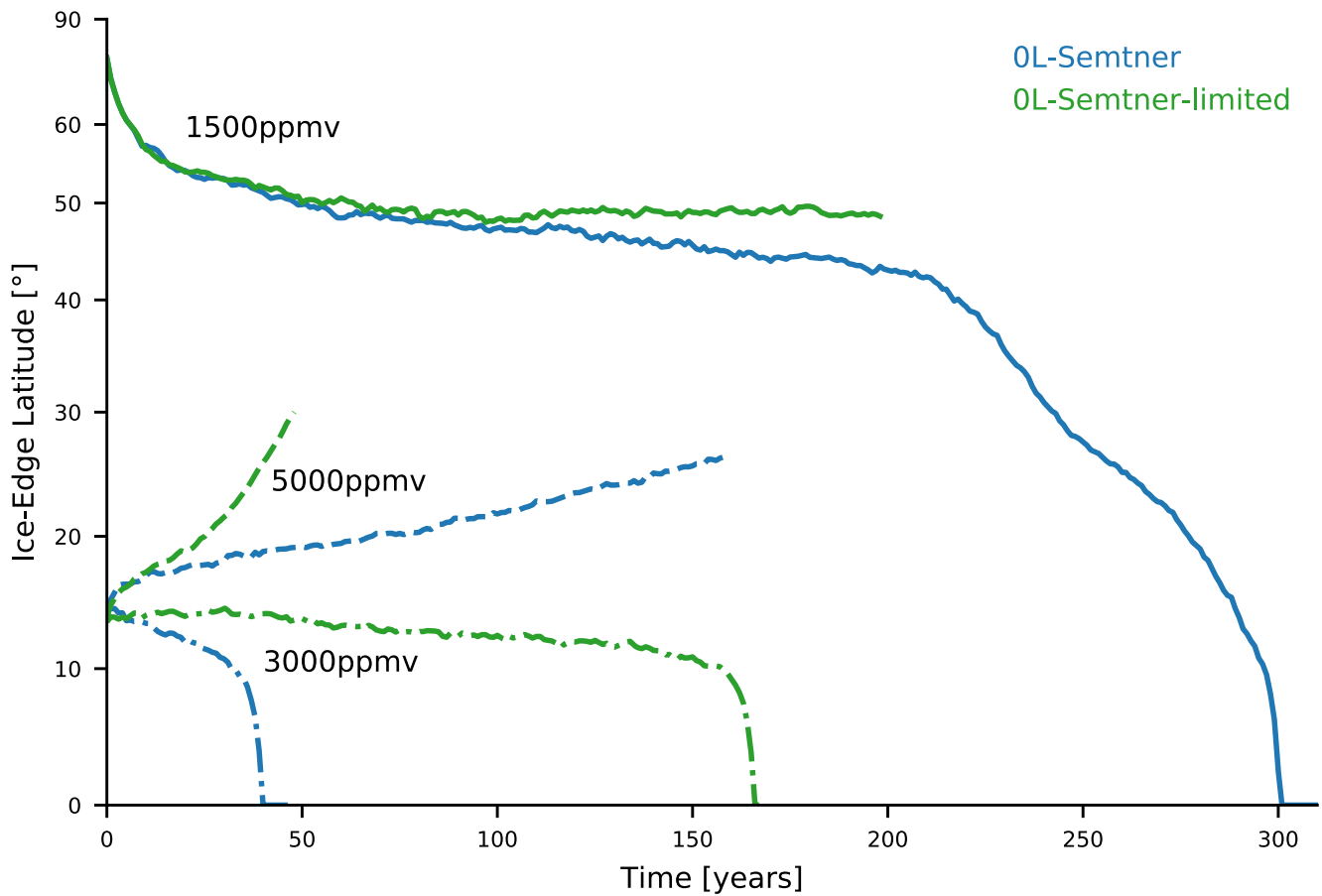$$\frac{dh_{i,r}}{dt} = \frac{F_r}{\rho_I L}. \tag{9}$$

Figure 11. Annual-mean latitude of the ice edge as a function of time for 0L-Semtner simulations with unlimited ice thickness (blue) and ice thickness limited to 5 m for three CO_2 values. The simulations with 1500 ppmv were started from an ice-free state, the other simulations from a transient simulation with an ice edge at 14°.

$h_{i,r}$ is normalized to the surface area and in units of m, F_r is in units of $W\,m^{-2}$. L is the latent heat of ice fusion and ρ_I is ice density. In our simulations we have diagnosed $h_{i,r}$ so that we can quantify F_r. Locally F_r increases with the temperature difference between the ocean and ice surface because this leads to stronger ice growth and more ice needs to be artificially melted. This is evident from Equation 7 of the 0L-Semtner scheme. The local heat flux does not depend on ice thickness since the latter is clamped at 5 m when the thickness limit is active.

On the global scale, the artificial heat flux increases with ice cover. This is shown by the scatter plot of ice edge and artificial heat flux in Figure 12. As long as ice is restricted to polar regions, the artificial heat flux is zero since ice has not yet grown to the thickness limit. As soon as ice expands to 60°, ice in the polar regions reaches the thickness limit and the artificial heat flux becomes non-zero. With growing ice cover the heat flux increases steadily. This can be explained by two factors. First, as ice cover grows, more regions reach the thickness limit. Second, as ice cover grows the temperature difference between the ocean and ice surface increases due to the cooling of the overall climate. Because of this, the heat flux increases somewhat stronger than expected from the increase of ice cover alone. Near the completion of global ice cover, the artificial heat flux increases substantially due to rapidly falling temperatures.

We put the artificial heat flux into perspective by converting it into the CO_2 increase that would be required to provide the same heat flux. For this, we use Myhre et al. (1998) and calculate the scaling factor between the actually used CO_2 and the higher CO_2 that would create the same artificial heat flux as the thickness limit. The scaling factor is given by

$$dCO_2 = \exp\left(\frac{F_r}{5.35\,\mathrm{W\,m^{-2}}}\right).$$
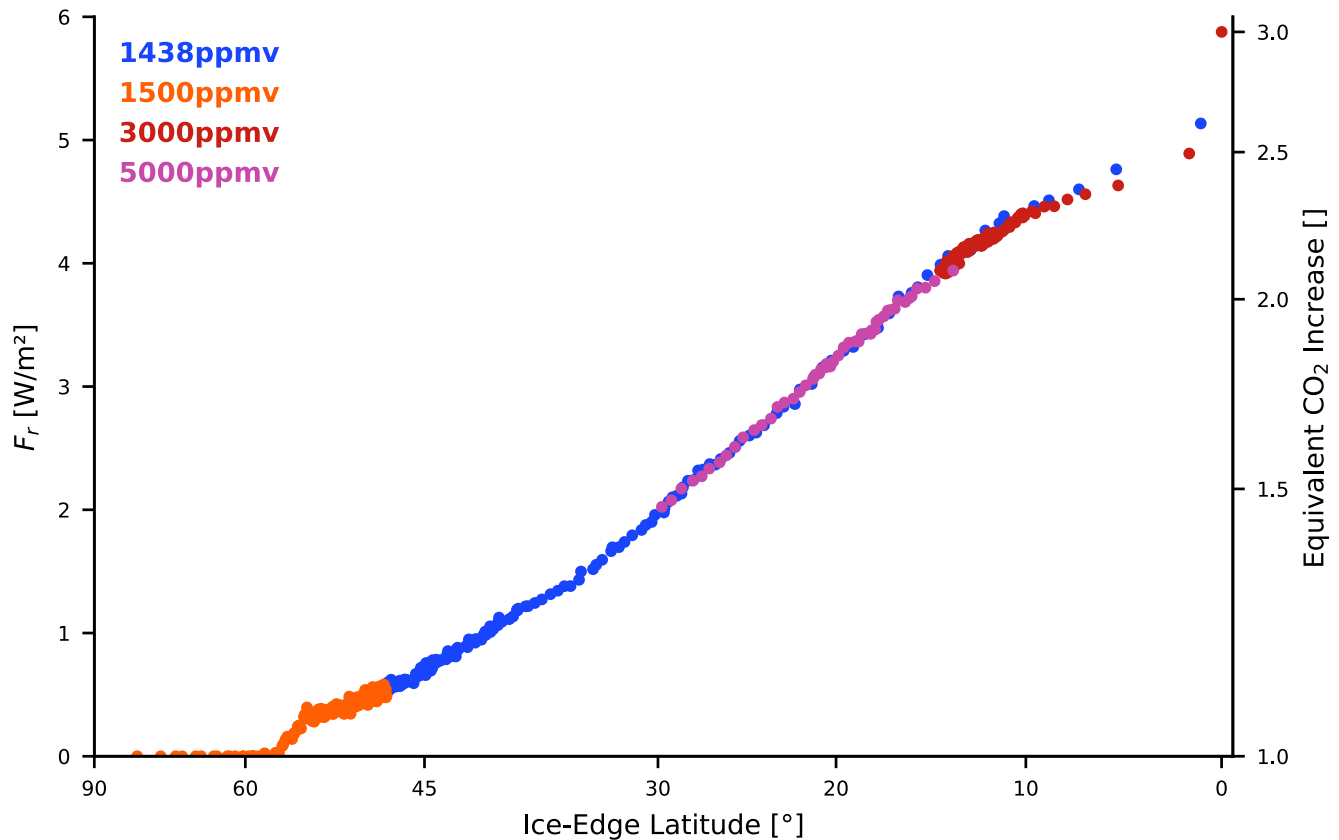
(10)

Figure 12. Scatter plot of the annual-mean global-mean artificial heat flux and the latitude of the ice edge in selected simulations with the 0L-Semtner scheme and ice thickness limited to 5 m. For the second y-axis on the right, the artificial heat flux is expressed in terms of an equivalent CO_2 increase (see text for details). Note that the latitude of the ice edge is plotted on a sine-scale. This is done to take into account for the increase in ice-covered area when the ice edge advances toward the equator.

For the simulation at 1500 ppmv, F_r reaches up to 0.5 W m^{-2} at the final ice latitude of 46.6° (see Figure 12). This corresponds to $dCO_2 = 1.1$ and means that for a simulation without ice thickness limitation a 10% higher CO_2, that is, 1650 ppmv, would be required to generate the same ice cover. This is in rough agreement with the difference in critical CO_2 between the 0L-Semtner scheme with and without thickness limitation.

For higher ice cover our assessment suggests a stronger impact. For states with an ice edge in the subtropics we estimate that the thickness limitation corresponds to a CO_2 change by a factor of two or more, indicating that it can lead to a substantial underestimation of the critical CO_2 for states with a stable subtropical ice edge (Abbot et al., 2011). This is for example, important for the coupled model study of Voigt and Abbot (2012) whose reported critical CO_2 can be expected to be biased low according to our analysis because ice thickness was limited to 8 m. At the same time, it is important to note that the thickness limit does not impact surface albedo, because it is not active near the ice edge (Figure 13) and there is no difference in snow cover.

5. Conclusion

We have presented a detailed and quantitative study on how sea ice thermodynamics affect Snowball Earth initiation. Many previous studies have analyzed the critical CO_2 and ice cover needed to trigger Snowball initiation in global climate models, and have analyzed a variety of factors that include for example, the continental distribution and the dynamics of the ocean, atmosphere and sea ice. Here, we complement these studies by specifically addressing how the representation of ice thermodynamics modulates the susceptibility of climate models to global glaciation.

To this end, we have compared two schemes for ice thermodynamics that are commonly implemented in models: the 3L-Winton scheme with 3 layers for snow and ice and an implicit representation of brine pockets, and the
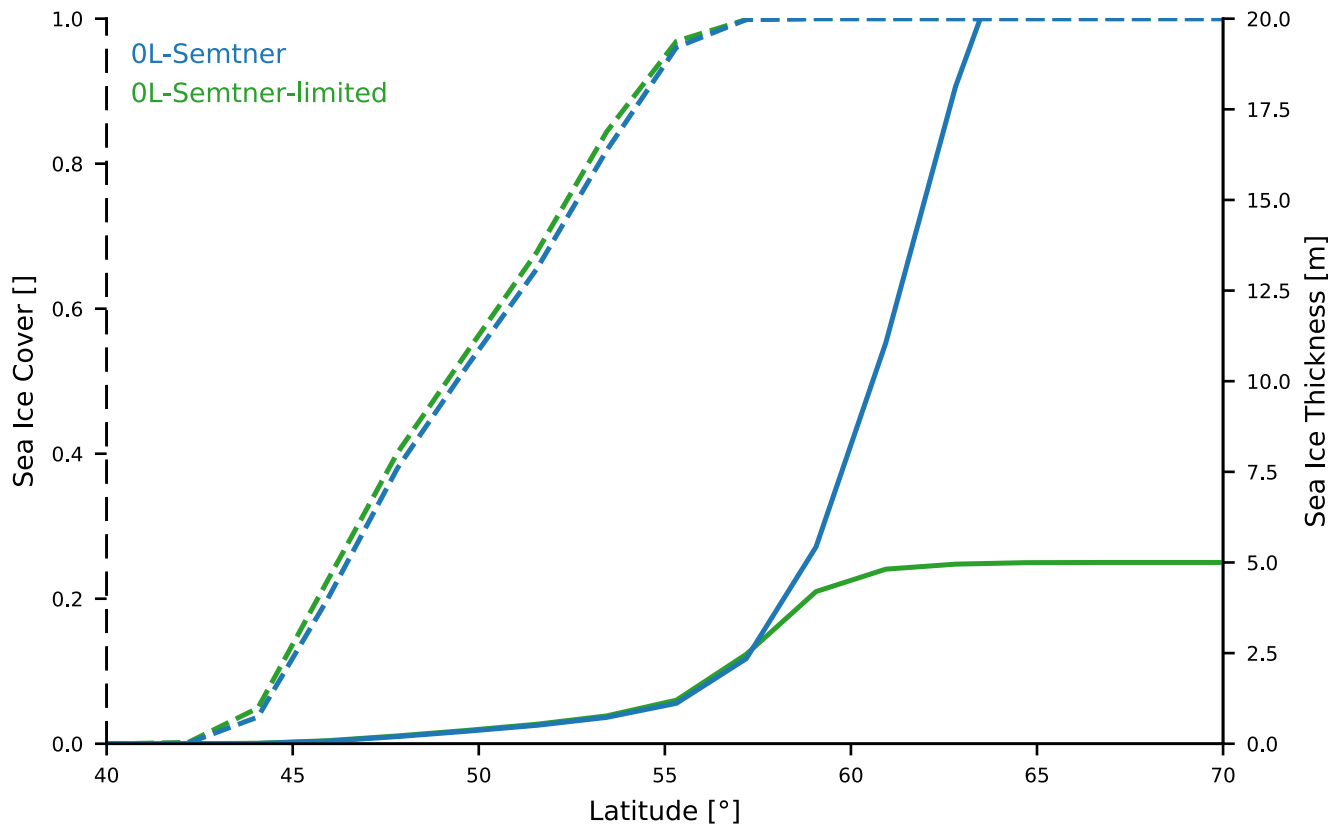
Figure 13. Zonal-mean ice cover (dashed lines) and ice thickness (solid lines) averaged over the final 40 years of 0L-Semtner simulations with and without ice thickness limited to 5 m (green and blue). The simulation with limited ice thickness is run with 1500 ppmv CO_2 and the one with unlimited ice thickness uses 1594 ppmv.

0L-Semtner scheme in which no internal layers are used and the energy storage in ice and snow is neglected. We have further used the 0L-Semtner scheme with ice thickness limited to 5 m. This is motivated by previous model studies in which ice thickness needed to be limited for technical reasons to avoid "dry" ocean levels (e.g., Voigt & Abbot, 2012; Voigt et al., 2011; Voigt & Marotzke, 2010). We have run a suite of simulations in idealized slab-ocean aquaplanet setup with zero ocean heat transport and different atmospheric CO_2. Based on these we have quantified the impact of ice thermodynamics on the critical CO2 content to trigger a Snowball event.

Initiating a Snowball is substantially easier when the heat capacity of ice and snow are taken into account, as is done in the 3L-Winton scheme. This results from a decrease in the magnitude of the diurnal cycle, which decreases daytime melting and weakens the melt-ratchet effect described by Abbot et al. (2010). The weaker diurnal cycle means that snow on ice survives longer into the summer season, which increases the surface albedo and contributes to the weakening of the ice albedo feedback. In the 0L-Semtner scheme, which assumes that ice responds instantaneously, Snowball initiation is more difficult due to the stronger diurnal and seasonal cycle of ice. Consequently, the critical CO_2 needed for Snowball initiation is 50% higher for the 3L-Winton scheme.

The impact of limiting ice thickness is secondary compared to the impact of vertical resolution. Limiting ice thickness changes the critical CO_2 by only 5%. The decrease in critical CO_2 arises from the imposed melting of ice that grows beyond the thickness limit, which leads to an artificial heat source that can be expressed as an effective increase in CO_2. The thickness limit only affects ice far from the ice edge and does not impact surface albedo, which explains why its impact is minor compared to vertical resolution.

Models are valuable tools to study the dynamics of climates very different from today. Yet, this comes with the challenge that they are applied in situations that are incongruent with assumptions and trade-offs made during their development. In today's climate ice is limited to a few meters and to high latitudes where the diurnal cycle is weak so that a 0-layer approximation can provide acceptable results. This is no longer true for much colder

climates in which ice becomes thicker and expands into regions with stronger diurnal variations in insolation. We acknowledge that the vertical resolution of the 3L-Winton scheme is still insufficient to properly resolve diurnal variations of ice temperature (Abbot et al., 2010; Yang et al., 2012b). Still, based on our results we recommend that future work on Snowball initiation should certainly take into account the energy storage in ice and snow since this strongly influences surface albedo and hence the magnitude of the ice-albedo feedback. In contrast, the thickness limitation is less crucial, as it does not impact surface albedo and its effect can be taken into account by rescaling the critical CO_2.

Our work has focused on stable ice edges in the midlatitudes around $50°$. This is due to the simple fact that ICON-A in the setup applied here does not exhibit stable states with ice edges closer to the equator (Braun et al., 2022). Some of our transient simulations indicate that the thermodynamics of sea ice can play an even stronger role as the ice edge moves into the subtropics and tropics. It would be interesting to study to what extent the stability of waterbelt states with a narrow strip of open ocean, as for example, described by Abbot et al. (2011), are affected by the treatment of the thermodynamics of sea ice. Based on what we have learned here we expect that the thickness limitation is rather inconsequential since the limit is not reached near the ice margin even in such states (Voigt & Abbot, 2012; Yang et al., 2012b). At the same time, it might be possible that increasing the vertical resolution of ice destabilizes waterbelt states by reducing seasonal ice melt near the ice edge.

Appendix A: Details of the Sea-Ice Model of Winton (2000)

A1. Heat Capacity of Ice Layers

A short description of the variable heat capacity in the model of Winton (2000) is given here. For a more detailed derivation, the reader is referred to Bitz and Lipscomb (1999) and Untersteiner (1961).

The enthalpy of upper-layer sea ice is defined as (cf. Equation 1 of Winton, 2000)

$$E_1(T_1) = C_0(T_1 + \mu S) - L\left(1 + \frac{\mu S}{T_1}\right). \tag{A1}$$

For the lower layer, where brine pockets are neglected, it is defined as (cf. Equation 25 of Winton, 2000)

$$E_2(T_2) = C_0(T_2 + \mu S) - L, \tag{A2}$$

C_0 is the (constant) heat capacity of ice, T_1 and T_2 are the internal ice temperatures of the upper and lower layer (in $°C$), S is the (constant) ice salinity, μ is an empirical factor relating ice salinity to its melting temperature, L is the latent heat of fusion. $L\frac{\mu S}{T_1}$ reduces the enthalpy of sea ice with increasing temperature, as a growing fraction of brine pockets will be present in the ice. Note that E_1 and E_2 are negative for reasonable temperature ranges.

The time derivative of the enthalpy results in (cf. Equation 2 of Winton, 2000)

$$m\frac{dE_1}{dt} = m\left(C_0 + \frac{L\mu S}{T_1^2}\right)\frac{dT_1}{dt} \tag{A3}$$

for the upper layer, and

$$m\frac{dE_2}{dt} = mC_0\frac{dT_2}{dt} \tag{A4}$$

for the lower layer. $C = C_0$ is thus the constant heat capacity of the lower ice layer, and $C = \left(C_0 + \frac{L\mu S}{T_1^2}\right)$ is the temperature dependent heat capacity of the upper ice layer. With higher temperatures close to the melting point, the heat capacity increases, as any change in temperature is accompanied by melting or freezing of internal brine pockets.

A2. Heat Flux Through the Coupled Snow-Ice Layer

The model of Winton (2000) does not consider internal snow temperatures. Therefore, the conductive heat flux to the surface originates from the midpoint of the upper ice layer up to the snow surface (see Figure 1a)). It runs

through half of the upper ice layer with the thickness $\frac{h_1}{2} = \frac{h_I}{4}$ and the conductivity k_I, as well as through the whole snow layer with the thickness h_S and conductivity k_S.

As the heat flux F_S through snow and ice is in equilibrium, it has to be the same as the heat fluxes through ice and snow respectively. Let T' be the temperature at the ice-snow interface, then the following applies for the heat flux through ice and snow:

$$F_S = k_{1/2} \frac{(T_1 - T_S)}{\frac{h_I}{4} + h_S} \tag{A5}$$

$$= k_I \frac{T_1 - T'}{\frac{h_I}{4}} \tag{A6}$$

$$= k_S \frac{T' - T_S}{h_S}, \tag{A7}$$

with the effective coupled conductivity of snow and ice $k_{1/2}$. Solving Equations A6 and A7 for T' results in

$$T' = \frac{k_I h_S T_1 + k_S \frac{h_I}{4} T_S}{k_I h_S + k_S \frac{h_I}{4}}. \tag{A8}$$

Substituting this into Equation A6.

$$F_S = \frac{k_I}{\frac{h_I}{4}} \left(T_1 - \frac{k_I h_S T_1 + k_S \frac{h_I}{4} T_S}{k_I h_S + k_S \frac{h_I}{4}} \right) \tag{A9}$$

$$= \frac{k_I}{\frac{h_I}{4}} \left(\frac{T_1 k_I h_S + T_1 k_S \frac{h_I}{4} - k_I h_S T_1 - k_S \frac{h_I}{4} T_S}{k_I h_S + k_S \frac{h_I}{4}} \right) \tag{A10}$$

$$= \frac{k_I}{\frac{h_I}{4}} \left(\frac{T_1 k_S \frac{h_I}{4} - T_S k_S \frac{h_I}{4}}{k_I h_S + k_S \frac{h_I}{4}} \right) \tag{A11}$$

$$= \frac{k_I k_S (T_1 - T_S)}{k_I h_S + k_S \frac{h_I}{4}} \tag{A12}$$

$$= \frac{T_1 - T_S}{\frac{h_S}{k_S} + \frac{h_I}{4 k_I}} \tag{A13}$$

results in the definition of the heat flux through ice and snow used in Equation 2.

Data Availability Statement

All data used in this study is available here: https://doi.org/10.25365/phaidra.304. ICON-A runscripts as well as all scripts used for postprocessing and analysis are available via gitlab hosted by the University of Vienna: https://gitlab.phaidra.org/climate/hoerner-seaice-james-2022.

References

Abbot, D. S., Eisenman, I., & Pierrehumbert, R. T. (2010). The importance of ice vertical resolution for snowball climate and deglaciation. *Journal of Climate*, *23*(22), 6100–6109. https://doi.org/10.1175/2010JCLI3693.1

Abbot, D. S., Voigt, A., & Koll, D. (2011). The Jormungand global climate state and implications for Neoproterozoic glaciations. *Journal of Geophysical Research*, *116*(D18103). https://doi.org/10.1029/2011JD015927

Bitz, C. M., & Lipscomb, W. H. (1999). An energy-conserving thermodynamic model of sea ice. *Journal of Geophysical Research: Oceans*, https://doi.org/10.1029/1999jc900100

Boucher, O., Servonnat, J., Albright, A. L., Aumont, O., Balkanski, Y., Bastrikov, V., et al. (2020). Presentation and evaluation of the IPSL-CM6A-LR climate model. *Journal of Advances in Modeling Earth Systems*, *12*(7), e2019MS002010. https://doi.org/10.1029/2019MS002010

Braun, C., Hörner, J., Voigt, A., & Pinto, J. (2022). Ice-free tropical waterbelt for Snowball Earth events questioned by uncertain clouds. *Nature Geoscience*, https://doi.org/10.1038/s41561-022-00950-1

Giorgetta, M. A., Brokopf, R., Crueger, T., Esch, M., Fiedler, S., Helmert, J., et al. (2018). ICON-A, the atmosphere component of the ICON Earth system model: I. Model description. *Journal of Advances in Modeling Earth Systems*, *10*(7), 1613–1637. https://doi.org/10.1029/2017MS001242

Hoffman, P. F., Abbot, D. S., Ashkenazy, Y., Benn, D. I., Brocks, J. J., Cohen, P. A., et al. (2017). Snowball Earth climate dynamics and Cryogenian geology-geobiology. *Science Advances*, *3*(11). https://doi.org/10.1126/sciadv.1600983

Hoffman, P. F., Kaufman, A. J., Halverson, G. P., & Schrag, D. P. (1998). A neoproterozoic Snowball Earth. *Science*, *281*(5381), 1342–1346. https://doi.org/10.1126/science.281.5381.1342

Jungclaus, J. H., Lorenz, S., Schmidt, H., Gutjahr, O., Haak, H., Mehlmann, C., et al. (2021). The ICON Earth system model version 1.0. *Journal of Advances in Modeling Earth Systems*.

Kirschvink, J. L. (1992). Late proterozoic low-latitude global glaciation: The Snowball Earth. In J. W. Schopf & C. Klein (Eds.) *The proterozoic biosphere: A multidisciplinary study* (pp. 51–52). Cambridge University Press.

Lewis, J. P., Weaver, A. J., & Eby, M. (2007). Snowball versus slushball Earth: Dynamic versus nondynamic sea ice? *Journal of Geophysical Research: Oceans*, *112*(C11). https://doi.org/10.1029/2006JC004037

Liu, P., Liu, Y., Peng, Y., Lamarque, J.-F., Wang, M., & Hu, Y. (2020). Large influence of dust on the Precambrian climate. *Nature Communications*, *11*(1), 4427. https://doi.org/10.1038/s41467-020-18258-2

Liu, Y., Peltier, W. R., Yang, J., & Hu, Y. (2018). Influence of surface topography on the critical carbon dioxide level required for the formation of a modern Snowball Earth. *Journal of Climate*, *31*(20), 8463–8479. https://doi.org/10.1175/JCLI-D-17-0821.1

Liu, Y., Peltier, W. R., Yang, J., & Vettoretti, G. (2013). The initiation of neoproterozoic "snowball" climates in CCSM3: The influence of paleo-continental configuration. *Climate of the Past*, *9*(6), 2555–2577. https://doi.org/10.5194/cp-9-2555-2013

Mauritsen, T., Bader, J., Becker, T., Behrens, J., Bittner, M., Brokopf, R., et al. (2019). Developments in the MPI-M Earth system model version 1.2 (MPI-ESM1.2) and its response to increasing CO2. *Journal of Advances in Modeling Earth Systems*, *11*(4), 998–1038. https://doi.org/10.1029/2018MS001400

Myhre, G., Highwood, E. J., Shine, K. P., & Stordal, F. (1998). New estimates of radiative forcing due to well mixed greenhouse gases. *Geophysical Research Letters*, *25*(14), 2715–2718. https://doi.org/10.1029/98GL01908

Pierrehumbert, R. T., Abbot, D. S., Voigt, A., & Koll, D. (2011). Climate of the neoproterozoic. *Annual Review of Earth and Planetary Sciences*, *39*(1), 417–460. https://doi.org/10.1146/annurev-earth-040809-152447

Poulsen, C. J., & Jacob, R. L. (2004). Factors that inhibit Snowball Earth simulation. *Paleoceanography and Paleoclimatology*, *19*(4). https://doi.org/10.1029/2004PA001056

Romanova, V., Lohmann, G., & Grosfeld, K. (2006). Effect of land albedo, CO_2, orography, and oceanic heat transport on extreme climates. *Climate of the Past*, *2*(1), 31–42. https://doi.org/10.5194/cp-2-31-2006

Rose, B. E. J. (2015). Stable "Waterbelt" climates controlled by tropical ocean heat transport: A nonlinear coupled climate mechanism of relevance to Snowball Earth. *Journal of Geophysical Research: Atmospheres*, *120*(4), 1404–1423. https://doi.org/10.1002/2014JD022659

Runnegar, B. (2000). Loophole for Snowball Earth. *Nature*, *405*(6785), 403–404. https://doi.org/10.1038/35013168

Semtner, A. J. (1976). A model for the thermodynamic growth of sea ice in numerical investigations of climate. *Journal of Physical Oceanography*, *6*(3), 379–389. https://doi.org/10.1175/1520-0485(1976)006<0379:amfttg>2.0.co;2

Sherwood, S. C., Bony, S., Boucher, O., Bretherton, C., Forster, P. M., Gregory, J. M., & Stevens, B. (2015). Adjustments in the forcing-feedback framework for understanding climate change. *Bulletin of the American Meteorological Society*, *96*(2), 217–228. https://doi.org/10.1175/BAMS-D-13-00167.1

Untersteiner, N. (1961). On the mass and heat budget of arctic sea ice. *Arch. Met. Geoph. Biokl. A.*, *12*(2), 151–182. https://doi.org/10.1007/BF02247491

Voigt, A., & Abbot, D. S. (2012). Sea-ice dynamics strongly promote Snowball Earth initiation and destabilize tropical sea-ice margins. *Climate of the Past*, *8*(6), 2079–2092. https://doi.org/10.5194/cp-8-2079-2012

Voigt, A., Abbot, D. S., Pierrehumbert, R. T., & Marotzke, J. (2011). Initiation of a Marnoun Snowball Earth in a state-of-the-art atmosphere-ocean general circulation model. *Climate of the Past*, *7*, 249–263. https://doi.org/10.5194/cp-7-249-2011

Voigt, A., & Marotzke, J. (2010). The transition from the present-day climate to a modern Snowball Earth. *Climate Dynamics*, *35*(5), 887–905. https://doi.org/10.1007/s00382-009-0633-5

Walsh, A., Ball, T., & Schultz, D. M. (2019). Extreme sensitivity in Snowball Earth formation to mountains on PaleoProterozoic supercontinents. *Scientific Reports*, *9*(1), 2349. https://doi.org/10.1038/s41598-019-38839-6

Winton, M. (2000). A reformulated three-layer sea ice model. *Journal of Atmospheric and Oceanic Technology*, *17*(4), 525–531. https://doi.org/10.1175/1520-0426(2000)017<0525:artlsi>2.0.co;2

Yang, J., Ji, W., & Zeng, Y. (2020). Transition from eyeball to snowball driven by sea-ice drift on tidally locked terrestrial planets. *Nature Astronomy*, *4*, 58–66. https://doi.org/10.1038/s41550-019-0883-z

Yang, J., Peltier, W. R., & Hu, Y. (2012a). The initiation of modern soft and hard Snowball Earth climates in CCSM4. *Climate of the Past*, *8*(3), 907–918. https://doi.org/10.5194/cp-8-907-2012

Yang, J., Peltier, W. R., & Hu, Y. (2012b). The initiation of modern "soft snowball" and "hard snowball" climates in CCSM3. Part I: The influences of solar luminosity, CO_2 concentration, and the sea ice/snow albedo parameterization. *Journal of Climate*, *25*(8). https://doi.org/10.1175/JCLI-D-11-00189.1